Article

Modeling of a Field-Modulated Permanent-Magnet Machine

Xianglin Li [1],*, K. T. Chau [2] and Yubin Wang [1]

[1] College of Information and Control Engineering, China University of Petroleum, Qingdao 266580, China; yubwang5190@163.com

[2] Department of Electrical and Electronic Engineering, The University of Hong Kong, Hong Kong, China; ktchau@eee.hku.hk

* Correspondence: xianglinli@upc.edu.cn; Tel.: +86-15066851211

Abstract: In this work, an effective field-modulated permanent-magnet (FMPM) machine was investigated, in which the spoke-magnet outer rotor and open-slot stator were employed. The objective of this paper is to provide the mathematical modeling analysis that was performed for the purpose of control research on this type of FMPM machine. The simulation results by means of finite element analysis (FEA) are given to verify the theoretical analysis and the validity of mathematical model. A prototype machine was also fabricated for experimentation. Both the analytical model and the FEA results are validated by experimental tests on the prototype machine.

1. Introduction

The operation of field-modulated permanent magnet (FMPM) machines relies on the "magnetic gearing effect" resulting from the magnetic field modulation [1], which can be derived from the coaxial magnetic gear by replacing the gear's high-speed rotor with a stationary armature fed by symmetrical three-phase winding currents [2]. It has been discussed that FMPM machines can develop a high torque density by using the high-speed armature field operation with low armature pole-pairs and slot number while the rotor still rotates at a low speed to transmit a high torque [3–5]. Due to the "magnetic gearing effect" coupled with its compact structure, high torque density, and high efficiency, the FMPM machine is promising for low-speed direct-drive applications such as wind power generation [6], wave energy conversion [7], and electric vehicles [8]. Recently, in order to verify the potential of FMPM machines for industry applications, many improved FMPM topologies have been successively proposed and analyzed [9,10]. Furthermore, in order to improve the power factor, a dual-stator spoke-magnet FMPM machine was developed and its attractive characteristics were demonstrated in [11].

The work of foregoing research on FMPM machines mainly focuses on the analysis of electromagnetic characteristics, such as achieving a high torque or force density, core loss calculation, magnetic circuit optimization, among others [12]. These analysis results have certainly confirmed the advantageous features of FMPM machines on torque capability and efficiency compared to traditional permanent magnet (PM) machines [13]. However, so far, a detailed modeling analysis of these FMPM machines prepared for the purpose of driving control has not been reported. It is known that the direct torque control or field-oriented control based on a synchronous *d-q* frame are commonly used for PM motor drive [14]. However, due to the "magnetic gearing effect", the rotational velocities of the PM rotor and armature field in an FMPM machine are different, thus it is necessary to discuss

how to define the synchronous *d-q* frame. Meanwhile, as a foundation for its driving control system, the mathematical modeling of FMPM machines based on the newly defined synchronous *d-q* frame should be established.

For this purpose, based on the previously presented spoke-magnet FMPM machine [15], this paper reports on the modeling analysis performed to build a foundation for its control system. In Section 2, the topology of the proposed FMPM machine will be introduced, and its operating principle is overviewed. In Section 3, the mathematical models developed based on stator frame and synchronous *d-q* frame will be described, and the finite element analysis (FEA) is also used for steady-state characteristics analysis, which serves as the basis of mathematical models. To verify the validity of modeling analysis, a prototype machine has been fabricated and its control system was also constructed, and the preliminary experimentation performance is discussed in Section 4. Finally, some conclusions are drawn in Section 5.

## 2. Topology and Operating Principle

2.1. Topology

Figure 1 shows the configurations of the proposed FMPM machine, in which the spoke-magnet outer rotor and open-slot stator are employed. An aluminum case is set outside the rotor by using a dovetail groove arrangement to fix rotor laminations for structural reliability. The spoke-magnets on the rotor are magnetized along the tangential direction, thus the flux-focusing effect can be obtained to greatly improve the air-gap flux density. Figure 1c shows the practical assembly diagram, in which there is a protective cover outside the rotating rotor for safety purposes and structural stability. There are 14 pole-pairs on the rotor and 18 slots on the stator, according to the pole-slot combination rules of FMPM machines [16,17], thus the stator windings need to be wound as 4 pole-pairs, which can be termed as an 18-slot/8-pole FMPM machine. That is, the stator pole pitch is 9/4 of the slot pitch. Hence, the three-phase symmetrical distributed windings consisting of 18 double-layer coils can be adopted, in which each coil span covers two slot pitches. In this case, the phase-winding factor is 0.945, and a sinusoidal back-electromotive force (EMF) can be developed.

(a)

(b)　　　　　　　　　　　　　　　(c)
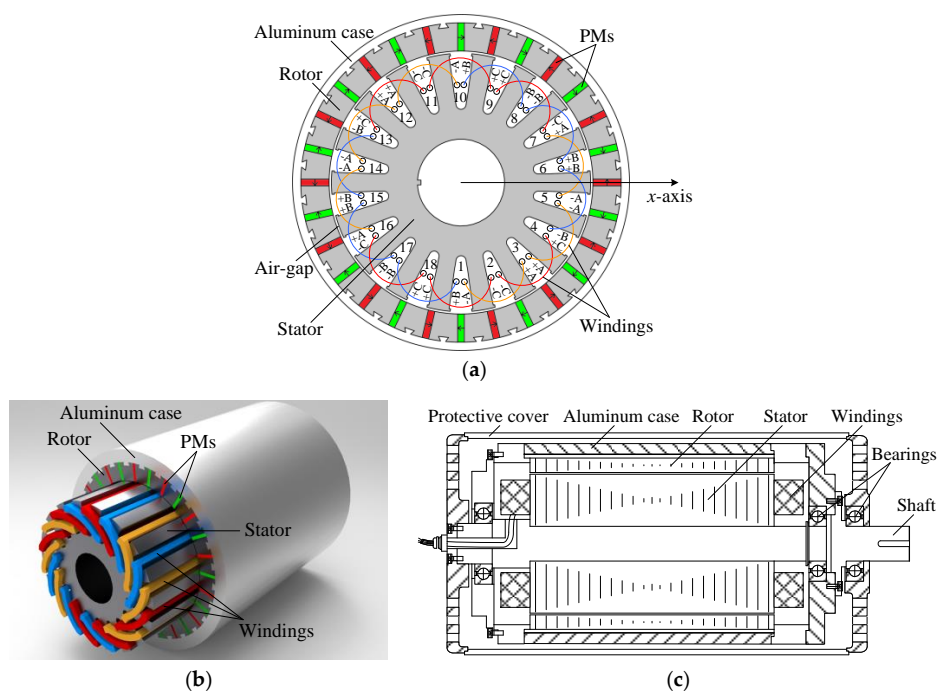
Figure 1. Configurations of the proposed field-modulated permanent-magnet (FMPM) machine. (**a**) Cross-section; (**b**) three-dimensional global model; and (**c**) assembly diagram.

2.2. Operating Principle

Figure 2 shows the open-circuit field distributions of the proposed machine at different rotor positions obtained by FEA. At the initial rotor position, as shown in Figure 2a, it can be seen that the directions of flux lines through the two stator teeth linked with coil A1 (or coil A2, or coil A3) are the same. Thus, the total flux linkage induced in coil A1, coil A2, and coil A3 of phase A reaches the positive maximum value at the initial position. When the rotor rotates 1/4 of the rotor pole-pair pitch counterclockwise to the position as shown in Figure 2b, the total flux linkage induced in coil A1, coil A2, and coil A3 will be nearly equal to zero. At rotor position $\theta_e = 180°$, as shown in Figure 2c, the directions of flux lines linked with coil A1, coil A2, and coil A3 are opposite to that generated at the initial position, thus the total flux linkage induced in coil A1, coil A2, and coil A3 reaches the maximum negative value. Also, at rotor position $\theta_e = 270°$, as shown in Figure 2d, the total flux linkage induced in coil A1, coil A2, and coil A3 becomes zero again. So, when the rotor rotates by one pole-pair pitch, a periodically changing flux linkage occurs in stator coils. However, it can be clearly seen from Figure 2 that the pole-pair number on the stator is much lower than the rotor magnet pole-pairs. It has been discussed that the stator tooth-slot alternation makes the circumferential air-gap permeance uneven, which results in this magnetic field modulation phenomenon. Therefore, in the proposed FMPM machine, the stator windings can be designed and wound by 4 pole-pairs to reduce complexity.

(a)　　　　　　　　(b)　　　　　　　　(c)　　　　　　　　(d)
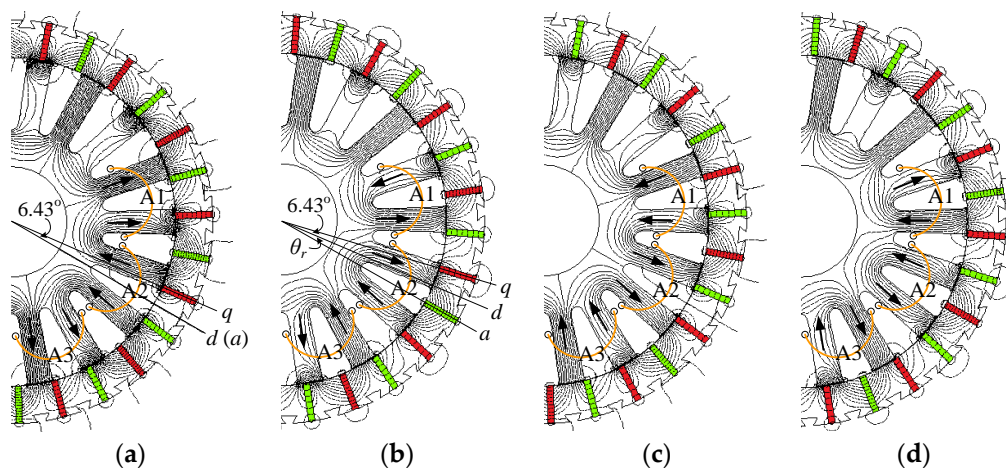
Figure 2. Open-circuit field distributions of the proposed 18-slot/8-pole FMPM machine at four different rotor positions, θ_e ("⟶" represents the direction of flux line). (**a**) $\theta_e = 0°$; (**b**) $\theta_e = 90°$; (**c**) $\theta_e = 180°$; and (**d**) $\theta_e = 270°$.

Figure 3a shows the no-load air-gap flux density of the proposed 18-slot/8-pole FMPM machine associated with Figure 1a, in which the initial condition of mechanical angle is aligned with *x*-axis. As depicted in [2,13], due to the field-modulation effect produced by the stator tooth-slot alternation, the air-gap flux density consists of a series of harmonic fields. By using Fourier transformation, the corresponding harmonic spectrum can be analyzed and is shown in Figure 3b. It can be seen that the 14 pole-pair rotor PM field and modulated 4 pole-pair harmonic field are prominent. Meanwhile, these two magnetic fields can be further modulated by the 18 stator teeth to generate distinct 24 pole-pair and 22 pole-pair harmonic fields, respectively. In fact, the electromechanical energy conversion in the proposed 18-slot/8-pole FMPM machine is undertaken by two sets of harmonics [13]. The first set is the 4 pole-pair stator fundamental and the PM subharmonic resulting from the interaction of the 14 pole-pair PM rotor and the 18 stator teeth. The second set is the interaction of the 14 pole-pair stator magnetomotive force (MMF) harmonic resulting from the modulation of the 4 pole-pair stator fundamental and the 18 stator teeth, and the 14 pole-pair rotor PM field. Due to the co-contribution of two sets of harmonics, a high torque density can be realized in the FMPM machine.
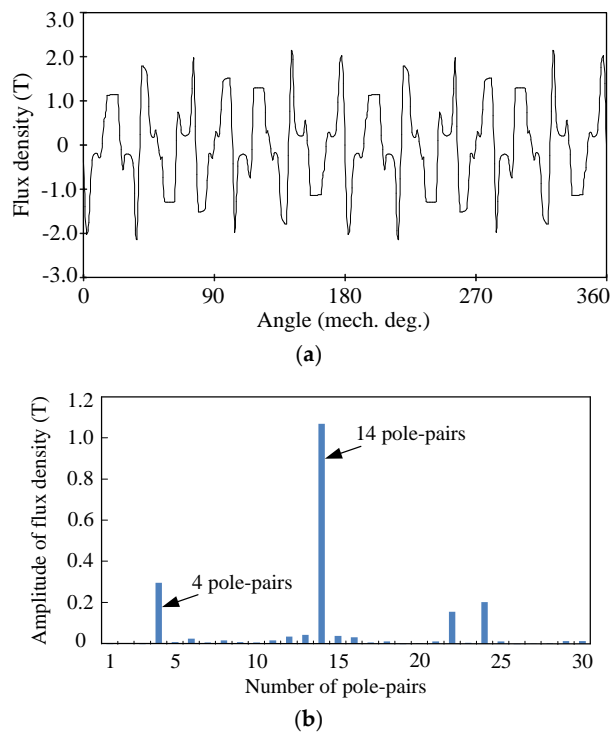
Figure 3. No-load air-gap flux density of the proposed 18-slot/8-pole FMPM machine. (**a**) Waveform; and (**b**) harmonic spectrum.

3. Mathematical Modeling

In the proposed machine, it can realize magnetic field modulation between rotor 14 pole-pairs and stator 4 pole-pairs, and both magnetic fields have different mechanical rotating velocities, namely, achieving the "magnetic gearing effect". However, taking the pole ratio G_r into account, both magnetic fields have the same electrical angular velocity ω_e. According to the 4 pole-pair field, the electric angle between adjacent slot EMF vectors is 80°; on the other hand, based on the 14 pole-pair field, it is 280°. That is, whether it is plotted based on a 4 pole-pair or 14 pole-pair field, the same slot EMF star diagram can be obtained as shown in Figure 4a,b, respectively. Hence, it also indicates that the "magnetic gearing effect" can make the 4 pole-pair and 14 pole-pair magnetic fields together contribute to the energy conversion, thus achieving significantly high torque capability in the proposed FMPM machine.
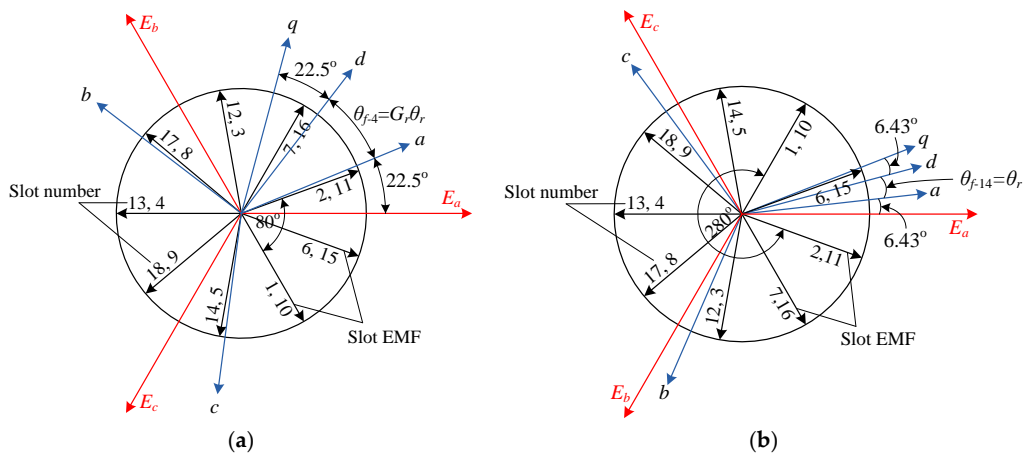
Figure 4. Slot electromotive force (EMF) star diagram and *d-q* axes definition of the proposed 18-slot/8-pole FMPM machine. (**a**) Based on 4 pole-pair field; and (**b**) based on 14 pole-pair field.

To realize the transformation from stator reference frame to rotor reference frame, the *d-q* axes of the proposed machine can be defined according to rotating 4 pole-pair field or 14 pole-pair field as shown in Figure 4a,b, respectively, in which $\theta_{f\text{-}4}$ and $\theta_{f\text{-}14}$ represent the mechanical angles of a 4 pole-pair field and a 14 pole-pair field relative to the initial position, respectively. As shown in Figure 2a, stator *a*-axis is defined along the central axis of phase A at the initial position where the PM flux linkage of phase A reaches the positive maximum value. Then, the initial *d*-axis is chosen to be consistent with *a*-axis, and the *q*-axis is 90° electrical degrees ahead of *d*-axis. The following relationship is governed in the proposed machine:

$$\begin{cases} \theta_{f-14} = \theta_r = \frac{1}{G_r}\theta_{f-4} \\ \theta_e = p_r\theta_r \\ G_r = \frac{p_r}{p_s} \end{cases} \tag{1}$$

where θ_r and θ_e are the mechanical and electrical angles of the rotor position, respectively; p_r and p_s are the pole-pair number of rotor and stator, respectively. It can be found that with the rotation of the rotor, the mechanical angles θ_{f-4} and θ_{f-14} are different due to the "magnetic gearing effect". However, their electrical angles are the same as θ_e. That is, the *d-q* axes definition based on 4 pole-pair field or 14 pole-pair field is in fact equivalent if it is treated from the viewpoint of electrical angle. Hence, to reduce confusion and simplify analysis, the following mathematical model is established based on the rotor electrical angle θ_e.

3.1. Mathematical Model in Stator Reference Frame

As shown in Figure 5a, the three-phase PM flux linkage of the proposed machine can be expressed as:

$$\begin{cases} \psi_{pma} = \psi_m \cos(\theta_e) \\ \psi_{pmb} = \psi_m \cos(\theta_e - 120^\circ) \\ \psi_{pmc} = \psi_m \cos(\theta_e + 120^\circ) \end{cases} \tag{2}$$

where ψ_m is the peak value of the phase PM flux linkage.
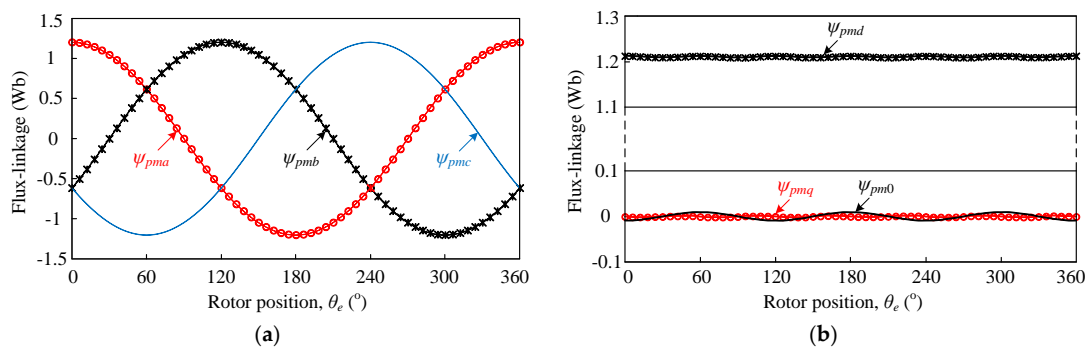
Figure 5. PM flux linkage of the proposed machine in different reference frames: (**a**) stator reference frame; (**b**) *d-q* reference frame.

Then, the total phase flux linkage excited by PMs and phase current on load can be expressed as:

$$\begin{bmatrix} \psi_a \\ \psi_b \\ \psi_c \end{bmatrix} = \begin{bmatrix} L_{aa} & M_{ab} & M_{ac} \\ M_{ba} & L_{bb} & M_{bc} \\ M_{ca} & M_{cb} & L_{cc} \end{bmatrix} \begin{bmatrix} i_a \\ i_b \\ i_c \end{bmatrix} + \begin{bmatrix} \psi_{pma} \\ \psi_{pmb} \\ \psi_{pmc} \end{bmatrix} \tag{3}$$

where i_a, i_b, and i_c are the phase currents, L_{aa}, L_{bb}, and L_{cc} are the phase self-inductances as shown in Figure 6a, and M_{ab}, M_{ac}, M_{ba}, M_{bc}, M_{ca}, and M_{cb} are the phase mutual inductances as shown in Figure 6b.
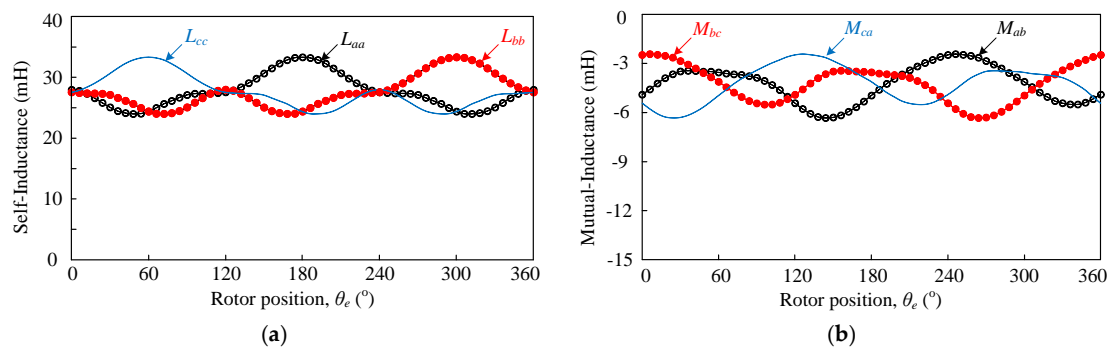
Figure 6. Self- and mutual-inductance of the proposed machine. (**a**) Self-inductance; and (**b**) mutual inductance.

Table 1 lists the characteristic information of inductance. It can be seen that the first and second harmonic components of self-inductance are significant, which account for around 10.1% and 6.7% of its DC component L_{DC}, respectively. Moreover, the DC component of mutual inductance M_{DC}, as shown in Table 1, is numerically about 16.4% of the self-inductance DC component L_{DC}, which should be taken into account. Although the fourth harmonic component of self-inductance and the second harmonic component of mutual inductance are not as negligible as all the other components, in order to facilitate the FMPM machine modeling, all these harmonic components are neglected. Thus, the phase inductance can be approximately expressed as:

$$\begin{cases} L_{aa} \approx L_{DC} - L_{m1}\cos(\theta_e) + L_{m2}\cos(2\theta_e) \\ L_{bb} \approx L_{DC} - L_{m1}\cos(\theta_e - 120°) + L_{m2}\cos\{2(\theta_e - 120°)\} \\ L_{cc} \approx L_{DC} - L_{m1}\cos(\theta_e + 120°) + L_{m2}\cos\{2(\theta_e + 120°)\} \\ M_{ab} = M_{bc} = M_{ca} = M_{ba} = M_{cb} = M_{ac} \approx M_{DC} \end{cases} \tag{4}$$

where L_{m1} and L_{m2} are the peak values of the first and second harmonic components of self-inductance, respectively.

Table 1. Inductance characteristics in stator reference frame.

Items	Self-Inductance		Mutual Inductance	
	Peak Value (mH)	Phase Angle	Peak Value (mH)	Phase Angle
DC component	28.711	-	−4.7168	-
First harmonic	2.9022	2.9°	0.8127	−76.5°
Second harmonic	1.9161	6°	1.353	−51.1°
Third harmonic	0.2063	9.3°	0.03	−72.7°
Fourth harmonic	1.2522	11.8°	0.289	71.3°
Fifth harmonic	0.0784	13.6°	0.1454	−13.4°

Thus, the voltage equations of the proposed machine in the stator reference frame can be written as:

$$\begin{bmatrix} u_a \\ u_b \\ u_c \end{bmatrix} = \begin{bmatrix} R_a & 0 & 0 \\ 0 & R_b & 0 \\ 0 & 0 & R_c \end{bmatrix} \begin{bmatrix} i_a \\ i_b \\ i_c \end{bmatrix} + \begin{bmatrix} \frac{d\psi_a}{dt} \\ \frac{d\psi_b}{dt} \\ \frac{d\psi_c}{dt} \end{bmatrix} \tag{5}$$

where R_a, R_b, and R_c are the phase resistances, which are equal due to symmetrical windings, thus termed as R. The power absorbed by the windings from the power supply can be expressed as:

$$P_i = u_a i_a + u_b i_b + u_c i_c \tag{6}$$

Substituting Equations (3) and (5) into Equation (6), and neglecting mutual inductances to simplify derivation, the electromagnetic torque of the proposed machine in stator reference frame can be derived as:

$$T_e = T_{pm} + T_r \tag{7}$$

in which:

$$T_{pm} = p_r \left(i_a \frac{d\psi_{pma}}{d\theta_e} + i_b \frac{d\psi_{pmb}}{d\theta_e} + i_c \frac{d\psi_{pmc}}{d\theta_e} \right) \tag{8}$$

$$T_r = \frac{p_r}{2} \left(i_a^2 \frac{dL_{aa}}{d\theta_e} + i_b^2 \frac{dL_{bb}}{d\theta_e} + i_c^2 \frac{dL_{cc}}{d\theta_e} \right) \tag{9}$$

where T_{pm} is the PM torque, and T_r is called the reluctance torque, which is caused by the fluctuation of the phase self-inductance with rotor positions.

3.2. Abc-dq Transformation

The vector-control strategy is based on the synchronous rotor frame, which rotates at the synchronous velocity. In order to get the two-phase rotary *d-q* axes electromagnetic parameters, the traditional Park matrix $P_{3s/2r}$ as shown in Equation (10) can be used for *abc-dq* transformation.

$$P_{3s/2r} = \frac{2}{3} \begin{bmatrix} \cos(\theta_e) & \cos(\theta_e - 120^\circ) & \cos(\theta_e + 120^\circ) \\ -\sin(\theta_e) & -\sin(\theta_e - 120^\circ) & -\sin(\theta_e + 120^\circ) \\ 1/2 & 1/2 & 1/2 \end{bmatrix} \tag{10}$$

Thus, the PM flux linkage in the *d-q* reference frame can be derived as:

$$\begin{bmatrix} \psi_{pmd} \\ \psi_{pmq} \\ \psi_{pm0} \end{bmatrix} = P_{3s/2r} \begin{bmatrix} \psi_{pma} \\ \psi_{pmb} \\ \psi_{pmc} \end{bmatrix} = \begin{bmatrix} \psi_m \\ 0 \\ 0 \end{bmatrix} \tag{11}$$

It can be seen from Equation (11) that the PM flux linkage in *d*-axis ψ_{pmd} is equal to the peak value of phase PM flux linkage in the stator reference frame. The PM flux linkages in *q*-axis ψ_{pmq} and in 0-axis ψ_{pm0} are equal to zero. To verify the aforementioned analysis, Figure 5b gives the PM flux linkage in the *d-q* reference frame, which is transformed from the three-phase PM flux linkage in the stator reference frame, as shown in Figure 5a, obtained by using FEA. The average value of ψ_{pmd}, ψ_{pmq}, and ψ_{pm0} are summarized in Table 2. It can be seen that the results calculated from the math model are consistent with the FEA.

Table 2. PM flux linkage in *d-q* reference frame. FEA: finite element analysis.

Items	Flux Linkage (Wb)	
	From FEA	**From Math Model**
ψ_{pmd}	1.2106	1.2031
ψ_{pmq}	−0.000079	0
ψ_{pm0}	−0.000173	0

Then, the inductances in *d-q* axes frame can be described as follows:

$$\begin{bmatrix} L_d & L_{dq} & L_{d0} \\ L_{qd} & L_q & L_{q0} \\ L_{0d} & L_{0q} & L_0 \end{bmatrix} = P_{3s/2r} \begin{bmatrix} L_{aa} & M_{ab} & M_{ac} \\ M_{ba} & L_{bb} & M_{bc} \\ M_{ca} & M_{cb} & L_{cc} \end{bmatrix} P_{3s/2r}^{-1} \tag{12}$$

where L_d, L_q, L_0, L_{dq}, L_{qd}, L_{d0}, L_{0d}, L_{q0}, and L_{0q} are the synchronous inductance components in *d-q* axes frame. Thus, by substituting Equations (4) and (10) into Equation (12), the synchronous inductance components in the *d-q* axes frame can be derived as:

$$L_d = L_{DC} - M_{DC} + \frac{L_{m2} - L_{m1}\cos(3\theta_e)}{2} \tag{13}$$

$$L_q = L_{DC} - M_{DC} - \frac{L_{m2} - L_{m1}\cos(3\theta_e)}{2} \tag{14}$$

$$L_0 = L_{DC} + 2M_{DC} \tag{15}$$

$$L_{dq} = L_{qd} = \frac{L_{m1}\sin(3\theta_e)}{2} \tag{16}$$

$$L_{d0} = 2 \times L_{0d} = -L_{m1} + L_{m2}\cos(3\theta_e) \tag{17}$$

$$L_{q0} = 2 \times L_{0q} = -L_{m2}\sin(3\theta_e) \tag{18}$$

It can be observed from Equations (13) and (14) that the *d*- and *q*-axis inductances, L_d and L_q, are not constant, both of which contain a small cosine component with three times variation frequency of the PM flux linkage. Generally, the mutual inductance between the *d*- and *q*-axis windings should be zero, because the flux induced by a current in one winding will not link with another winding displaced in space by 90° electrical degrees. However, in the PM machine with salient rotor and stator teeth, a part of the *d*-axis winding flux will link with the *q*-axis winding due to the fact that the uneven reluctance provides a path for flux through the *q*-axis winding [18]. For the proposed machine, the spoke-magnet rotor can produce a certain "salient effect". Hence, the *d*- and *q*-axis mutual inductance L_{dq} is not zero; rather, it is a small sinusoidal waveform and equal to L_{qd}.

To validate the aforementioned equations, Figure 7a shows the self-inductance components in *d-q* axes frame, L'_d, L'_q, and L'_0, which are transformed directly from the three-phase inductances in the stator frame, as shown in Figure 6, obtained by using FEA. On the other hand, by substituting the DC components of the inductances (L_{DC}, M_{DC}) and the peak value of harmonic components of the inductances (L_{m1}, L_{m2}) listed in Table 1 into Equations (13)–(15), the self-inductance in the *d-q* axes frame, L_d, L_q, and L_0 can also be calculated and comparatively shown in Figure 7a. Meanwhile, Figure 7b compares the mutual inductance components in *d-q* axes frame, L'_{dq}, and L_{dq} obtained by the aforementioned two methods, respectively. It can be seen from Figure 7 that there are some minor differences between L_d and L'_d, L_q and L'_q, L_0 and L'_0, but the variation shape is nearly the same. Moreover, the average values are L_d = 34.33 mH, L_q = 32.47 mH, L'_d = 35.35 mH, L'_q = 31.58 mH, and $L_0 = L'_0$ = 19.3 mH as listed in Table 3. It can be seen that the results are in good agreement.
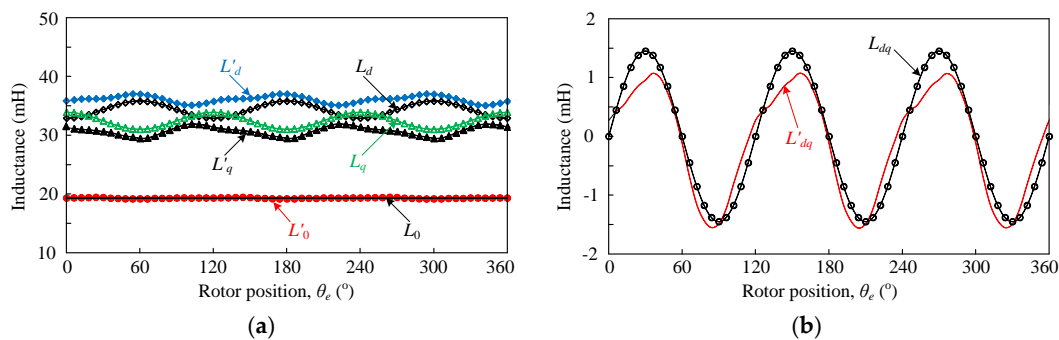
Figure 7. Waveforms of inductance. (**a**) Self-inductance in *d-q* axes frame, L_d, L_q, L_0, L'_d, L'_q, and L'_0; and (**b**) mutual inductance in *d-q* axes frame, L_{dq} and L'_{dq}.

Table 3. Average values of inductance in *d-q* axes frame.

Items	Average Values of Inductance (mH)		
	From FEA	**From Math Model**	**From [19]**
L'_d (L_d)	35.35	34.33	33.68
L'_q (L_q)	31.58	32.47	30.72
L'_0 (L_0)	19.3	19.3	-
L'_{dq} (L_{dq})	−0.094	0	-

In order to verify the inductance expressions in *d-q* axes frame, the calculation method of *d-q* frame inductance, as discussed in [19], can also be adopted, namely:

$$L_d = \frac{\psi_i \cos \alpha - \psi_{pm}}{I_d} \tag{19}$$

$$L_q = \frac{\psi_i \sin \alpha}{I_q} \tag{20}$$

where ψ_i is the fundamental component of the total flux linkage considering the armature reaction effect, ψ_{pm} is the fundamental component of the flux linkage excited by PMs only, and α is the phase difference between ψ_i and ψ_{pm}. Based on Equations (19) and (20), the *d-q* frame inductances are L_d = 33.68 mH and L_q = 30.72 mH, as listed in Table 3. It can be seen that the calculated inductances in the *d-q* reference frame are nearly the same as the results obtained from the proposed mathematical method and the FEA.

3.3. Electromagnetic Torque

Based on the preceding analysis, and assuming that the zero-sequence current component is equal to zero, the total flux linkage in *d-q* reference frame can be defined as:

$$\begin{cases} \psi_d = \psi_{pmd} + L_d i_d + L_{dq} i_q \\ \psi_q = L_q i_q + L_{dq} i_d \end{cases} \tag{21}$$

Substituting Equations (11), (13), (14), and (16) into Equation (21), it yields:

$$\begin{cases} \psi_d = \psi_m + \left(L_{DC} - M_{DC} + \dfrac{L_{m2} - L_{m1} \cos(3\theta_e)}{2} \right) i_d + \left(\dfrac{L_{m1} \sin(3\theta_e)}{2} \right) i_q \\ \psi_q = \left(L_{DC} - M_{DC} - \dfrac{L_{m2} - L_{m1} \cos(3\theta_e)}{2} \right) i_q + \left(\dfrac{L_{m1} \sin(3\theta_e)}{2} \right) i_d \end{cases} \tag{22}$$

In order to prove the accuracy of Equation (22), the flux linkage in the *d*- and *q*-axis are calculated by two methods and compared in Figure 8, where "ψ_d_FEA" and "ψ_q_FEA" denote the total flux linkage in *d*- and *q*-axis, obtained by using FEA, when i_d=0 control strategy is adopted at the rated current, "ψ_d_Math model" and "ψ_q_Math model" denote the total flux linkage in *d*- and *q*-axis calculated by Equation (22). It can be seen that the shape and value of the *d-q* axes frame flux linkage based on these two methods are nearly the same.
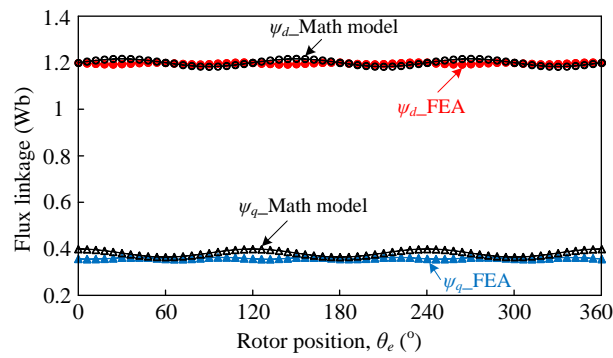
Figure 8. Waveforms of the flux linkage in *d-q* axes frame under $i_d = 0$ control.

The voltage equations in the *d*- and *q*-axis can be written as:

$$\begin{cases} u_d = Ri_d + \dfrac{d\psi_d}{dt} - \omega_e\psi_q \\ u_q = Ri_q + \dfrac{d\psi_q}{dt} + \omega_e\psi_d \end{cases} \tag{23}$$

Based on Equation (23), the electromagnetic torque of the proposed machine in *d-q* reference frame can be derived as:

$$\begin{aligned} T_e &= \frac{3}{2}\frac{\omega_e\left(\psi_d i_q - \psi_q i_d\right)}{\omega_r} \\ &= \frac{3p_r}{2}\left[\psi_m i_q + i_d i_q\left(L_d - L_q\right) + L_{dq}\left(i_q^2 - i_d^2\right)\right] \\ &= T_{pm} + T_r \end{aligned} \tag{24}$$

where ω_r is the rotor mechanical angular velocity. Substituting Equations (1), (13), (14), and (16) into Equation (24) yields:

$$T_{pm} = \frac{3}{2}G_r p_s \psi_m i_q \tag{25}$$

$$T_r = \frac{3}{2}G_r p_s i_d i_q\left[L_{m2} - L_{m1}\cos(3\theta_e)\right] + \frac{3}{4}G_r p_s L_{m1}\left(i_q^2 - i_d^2\right)\sin(3\theta_e) \tag{26}$$

Obviously, the reluctance torque T_r is the result of L_{m1}, L_{m2} due to the fluctuation of phase inductance, which can cause torque ripple.

When $i_d = 0$ control method is adopted, then the three-phase currents are applied in phase with the back-EMF, which can be expressed as:

$$\begin{cases} i_a = I_m\sin(\theta_e) \\ i_b = I_m\sin(\theta_e - 120^{\mathrm{o}}) \\ i_c = I_m\sin(\theta_e + 120^{\mathrm{o}}) \end{cases} \tag{27}$$

where I_m is the peak value of the phase current. Thus, the phase current in *d*- and *q*-axis can be transformed as:

$$\begin{cases} i_d = 0 \\ i_q = I_m \\ i_0 = 0 \end{cases} \tag{28}$$

By substituting Equation (28) into Equation (24), the electromagnetic torque can be derived as:

$$T_e = \frac{3}{2} G_r p_s \left[\psi_m I_m + \frac{I_m^2 L_{m1} \sin(3\theta_e)}{2} \right] \tag{29}$$

It can be seen from Equation (29) that the electromagnetic torque consists of two components, namely a DC component and a sinusoidal component with three times variation frequency of the PM flux linkage. Hence, the torque ripple can be defined as:

$$K_{\text{ripple}} = \frac{T_{e\max} - T_{e\min}}{T_{e\text{avg}}} \times 100\% = \frac{L_{m1} I_m}{\psi_m} \times 100\% \tag{30}$$

where $T_{e\max}$, $T_{e\min}$, and $T_{e\text{avg}}$ are the maximum value, the minimum value, and the average value of the electromagnetic torque, respectively. Equation (30) also denotes that the torque ripple is proportional to the peak value of the phase current.

By substituting $G_r = 3.5$, $p_s = 4$, $\psi_m = 1.2031$ Wb, $I_m = 8.3 \times 1.414$ A, $L_{m1} = 2.9022$ mH into Equation (29), the electromagnetic torque of the proposed 18-slot/8-pole FMPM machine can be calculated and noted as "T_e_Math model", as shown in Figure 9. To verify the aforementioned mathematical analysis, the electromagnetic torque of the proposed machine can also be obtained by using FEA and termed as "T_e_FEA", which is simultaneously described in Figure 9. Table 4 lists the key characteristics of "T_e_Math model" and "T_e_FEA". It can be seen that the average value of "T_e_Math model" and "T_e_FEA" are nearly the same, and the torque ripple of the proposed machine is less than 3%. However, it should be noted that the periodicity of the "T_e_Math model" is different from that of the "T_e_FEA". This is mainly due to neglecting the higher-order harmonic components in the mathematically calculated inductance.

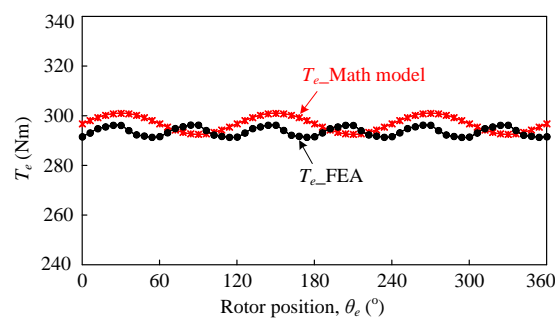**Figure 9.** Electromagnetic torque waveforms.

Table 4. Characteristics of electromagnetic torque.

| Items	T_e_**Math Model**	T_e_**FEA**
$T_{e\max}$ (Nm)	301.8	296.1
$T_{e\min}$ (Nm)	293.4	291.1
$T_{e\text{avg}}$ (Nm)	297.6	293.4
K_{ripple} (%)	2.8	1.7

4. Experimental Results

To validate the mathematical model and associated FEA analysis of the proposed machine, a prototype machine has been fabricated for experimentation as shown in Figure 10. The detailed specifications and main design parameters are listed in Table 5. Figure 11 illustrates and compares the measured self-inductance with the calculated self-inductance by means of FEA. The measured inductance waveforms agree well with the simulated results. The measured average phase self-inductance is about 27.1 mH, which is near to the calculated value 28.7 mH.

(**a**)   (**b**)   (**c**)

Generator

Prototype Machine

(**d**)
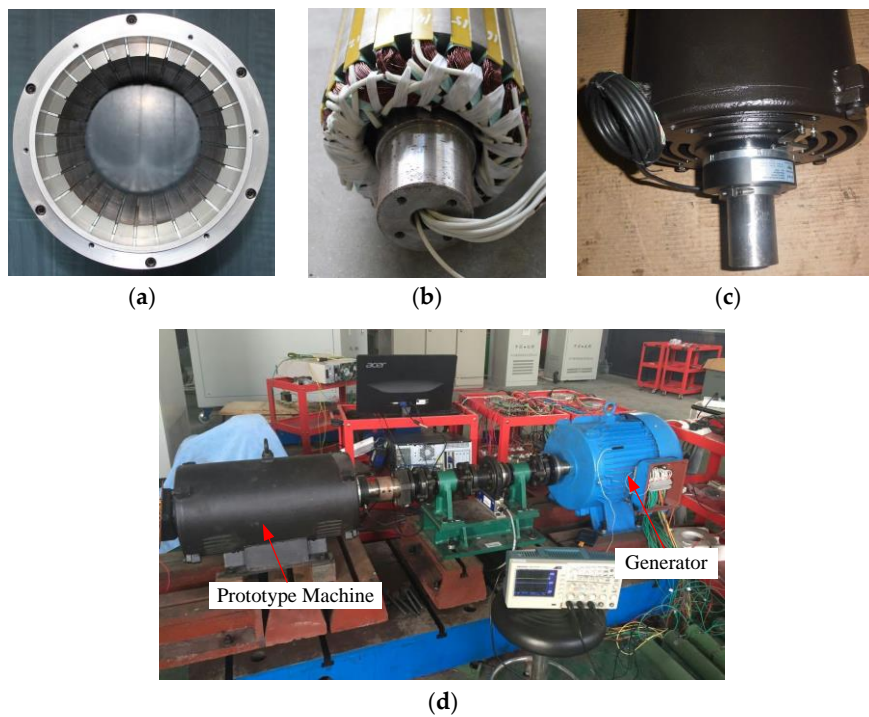
Figure 10. Prototype of proposed 18-slot/8-pole FMPM machine. (**a**) Outer rotor; (**b**) stator; (**c**) prototype assembly; and (**d**) experimental setup.

**Table 5.** Design specifications of the prototype machine.

Parameters	Values	Parameters	Values
Rated speed (r/min)	172	Outer diameter of rotor (mm)	220
Back-EMF (V)	220	Inner diameter of stator (mm)	60
Rated current (A)	8.3	Air-gap length (mm)	0.5
No. of rotor pole-pairs	14	Stack length (mm)	300
No. of stator teeth	18	Iron lamination material	DW470
No. of stator pole-pairs	4	PM material	N38SH
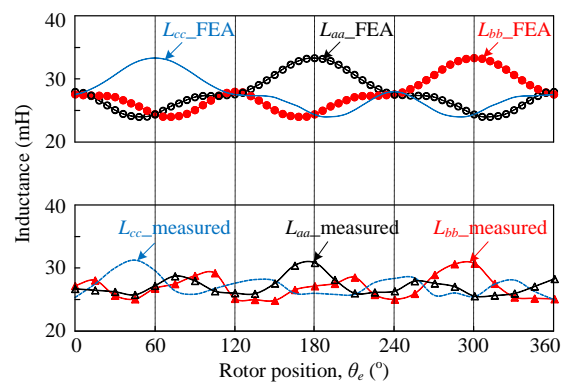
Figure 11. Comparison of measured and simulated self-inductances.

Also, the simulation and measured open-circuit back-EMF at the rated speed 172 r/min are shown in Figure 12. The phase back-EMF root mean square (RMS) values of simulation and experimental results are 224 V and 220 V, respectively, and the corresponding total harmonic distortion (THD) are

3.8% and 3%, respectively. It can be found that the experimental results exhibit a good agreement with the simulation results.
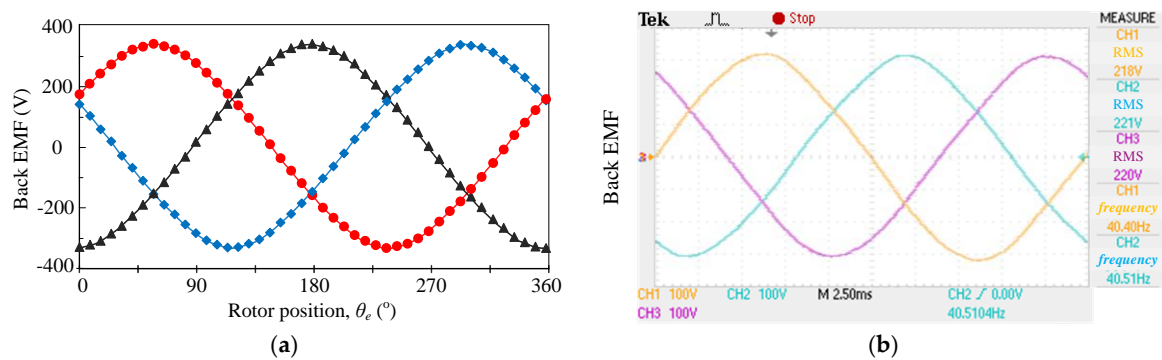
Figure 12. Back-EMF waveforms at the rated speed. (**a**) Finite element analysis (FEA) results; and (**b**) experimental results (100 V/div).

Based on the aforementioned modeling analysis, the vector-control strategy can be applied for the prototype machine. Figure 13a shows the variations of output torque and speed with sudden increased load from 115 Nm to 180 Nm at the rated speed 172 r/min, and the corresponding variations of the three-phase current are given in Figure 13b. It can be seen that the output torque can rapidly track the load changes, and the torque ripples at steady state are always very low.
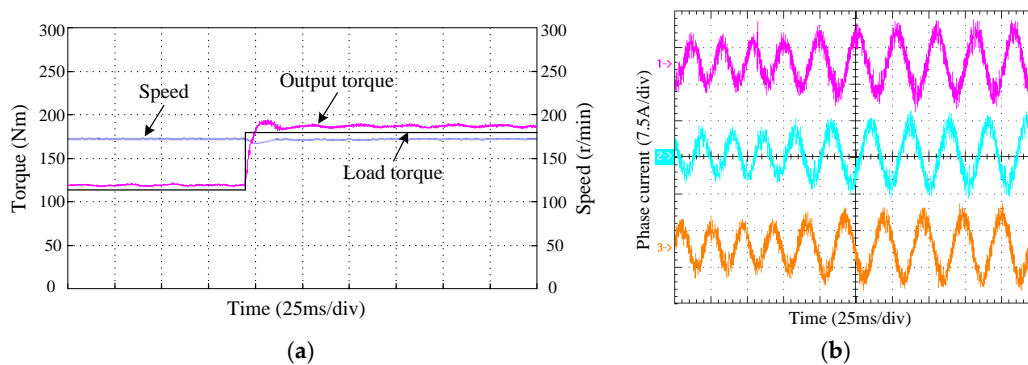
Figure 13. Performance characteristics of the prototype machine with sudden increased load at the rated speed. (**a**) Output torque and speed variations; and (**b**) three-phase current variation.

In the experiments, the input power can be calculated by the measured input voltage and current, and the output power can be calculated by the measured output torque and rotor speed. Thus, the efficiency of the prototype machine can be obtained as shown in Figure 14. It can be observed that the prototype efficiency improves as the load increases. When the output torque achieves 255 Nm, namely the rated phase current 8.3A is reached, the measured prototype efficiency is about 0.92. Under this rated condition, the measured power factor of the prototype machine is about 0.87, which is consistent with the conclusion drawn in the dual-stator spoke-array vernier PM machine presented in [20], indicating that the spoke-magnet rotor arrangement can effectively improve the power factor of the proposed FMPM machine. Without considering the mechanical and stray losses, the transmitted torque per total volume of the prototype machine is up to 22.4 kNm/m^3 under the naturally cooled condition.

Furthermore, in order to achieve perfect operation performance, improved control algorithms are still under testing for the control system. The corresponding experimental results will be the substance for our future paper.
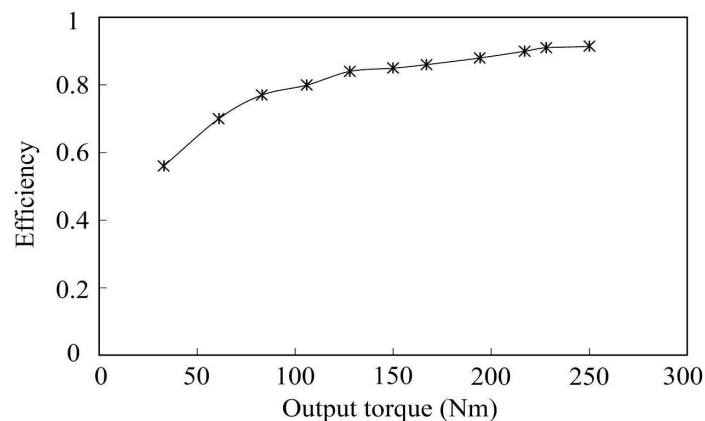
Figure 14. Measured efficiency of prototype machine.

5. Conclusions

In this work, the structure, operating principle, and the static characteristics of a new field-modulated PM machine have been investigated. Based on the static characteristics, the mathematical model of flux-linkage, inductance, and electromagnetic torque in the stator reference frame has been built. By using Park's transformation, the *d*- and *q*-components of flux-linkage, inductance, voltage, and electromagnetic torque in the *d-q* reference frame have been derived. The electromagnetic performances based on the mathematical models are also verified by FEA results. To validate the theoretical analysis, a prototype machine has been built and tested. The experimental results are in satisfactory agreement with the predicted results from the FEA and mathematical models. Therefore, it can be concluded that the mathematical modeling analysis of the proposed FMPM machine has formed a foundation for future study in vector-control or direct-torque control for this type of FMPM machines.

Author Contributions: Xianglin Li mainly conducted the modeling analysis of the proposed field-modulated permanent-magnet machine and performed the experiments. The manuscript was improved and revised by K. T. Chau and Yubin Wang. All of the authors contributed to the paper writing.

Conflicts of Interest: The authors declare no conflict of interest.

References

1. Toba, A.; Lipo, T.A. Generic torque-maximizing design methodology of surface permanent-magnet vernier machine. *IEEE Trans. Ind. Appl.* **2000**, *36*, 1539–1546.
2. Atallah, K.; Calverley, S.D.; Howe, D. Design, analysis and realization of a high-performance magnetic gear. *IEE Proc. Electr. Power Appl.* **2004**, *151*, 135–143. [CrossRef]
3. Niu, S.X.; Ho, S.L.; Fu, W.N.; Wang, L.L. Quantitative comparison of novel vernier permanent magnet machines. *IEEE Trans. Magn.* **2010**, *46*, 2032–2035. [CrossRef]
4. Vukotić, M.; Miljavec, D. Design of a permanent-magnet flux-modulated machine with a high torque density and high power factor. *IET Electr. Power Appl.* **2016**, *10*, 36–44. [CrossRef]
5. Zheng, P.; Song, Z.Y.; Bai, J.G.; Tong, C.D.; Yu, B. Research on an axial magnetic-field-modulated brushless double rotor machine. *Energies* **2013**, *6*, 4799–4829. [CrossRef]
6. Luo, X.; Niu, S.X. Maximum power point tracking sensorless control of an axial-flux permanent magnet vernier wind power generator. *Energies* **2016**, *9*, 581. [CrossRef]
7. Du, Y.; Cheng, M.; Chau, K.T.; Liu, X.; Xiao, F.; Zhao, W. Linear primary permanent magnet vernier machine for wave energy conversion. *IET Electr. Power Appl.* **2015**, *9*, 203–212. [CrossRef]

8. Cheng, M.; Sun, L.; Buja, G.; Song, L. Advanced electrical machines and machine-based systems for electric and hybrid vehicles. *Energies* **2015**, *8*, 9541–9564. [CrossRef]

9. Cheng, M.; Zhu, Y. The state of the art of wind energy conversion systems and technologies: A review. *Energy Convers. Manag.* **2014**, *88*, 332–347. [CrossRef]

10. Wang, Q.; Niu, S.X.; Ho, S.L.; Fu, W.N.; Zuo, S. Design and analysis of novel magnetic flux-modulated mnemonic machines. *IET Electr. Power Appl.* **2015**, *9*, 469–477. [CrossRef]

11. Li, D.W.; Qu, R.H.; Lipo, T.A. High-power-factor vernier permanent magnet machines. *IEEE Trans. Ind. Appl.* **2014**, *50*, 3664–3674. [CrossRef]

12. Jian, L.N.; Xu, G.Q.; Mi, C.C.; Chau, K.T.; Chan, C.C. Analytical method for magnetic field calculation in a low-speed permanent-magnet harmonic machine. *IEEE Trans. Energy Convers.* **2011**, *26*, 862–870. [CrossRef]

13. Li, X.L.; Chau, K.T.; Cheng, M.; Kim, B.; Lorenz, R.D. Performance analysis of a flux-concentrating field-modulated permanent-magnet machine for direct-drive applications. *IEEE Trans. Magn.* **2015**, *51*. [CrossRef]

14. Shao, L.Y.; Hua, W.; Dai, N.Y.; Tong, M.H.; Cheng, M. Mathematical modeling of a 12-phase flux-switching permanent-magnet machine for wind power generation. *IEEE Trans. Ind. Electron.* **2016**, *63*, 504–516. [CrossRef]

15. Li, X.L.; Chau, K.T.; Cheng, M. Analysis, design and experimental verification of a field-modulated permanent-magnet machine for direct-drive wind turbines. *IET Electr. Power Appl.* **2015**, *9*, 150–159. [CrossRef]

16. Wu, L.L.; Qu, R.H.; Li, D.W.; Gao, Y.T. Influence of pole ratio and winding pole numbers on performance and optimal design parameters of surface permanent-magnet vernier machines. *IEEE Trans. Ind. Appl.* **2015**, *51*, 3707–3715. [CrossRef]

17. Kim, B.; Lipo, T.A. Operation and design principles of a PM vernier motor. *IEEE Trans. Ind. Appl.* **2014**, *50*, 3656–3663. [CrossRef]

18. Krishnan, R. *Permanent Magnet Synchronous and Brushless DC Motor Devices*; CRC Press: Boca Raton, FL, USA, 2010.

19. Kim, S.; Lee, G.H.; Hong, J.P.; Jung, T.U. Design process of interior PM synchronous motor for 42-V electric air-conditioner system in hybrid electric vehicle. *IEEE Trans. Magn.* **2008**, *44*, 1590–1593.

20. Li, D.W.; Qu, R.H.; Xu, W.; Li, J.; Lipo, T.A. Design procedure of dual-stator spoke-array vernier permanent-magnet machines. *IEEE Trans. Ind. Appl.* **2015**, *51*, 2972–2983. [CrossRef]